Research Square

Preprints are preliminary reports that have not undergone peer review.
They should not be considered conclusive, used to inform clinical practice,
or referenced by the media as validated information.

Atomic-Scale Quantum Control of Single Spin Defects in a Two-Dimensional Semiconductor

Philip Willke

philip.willke@kit.edu

Karlsruhe Institute of Technology (KIT) https://orcid.org/0000-0002-7215-8419

Kwan Ho Au-Yeung

Karlsruhe Institute of Technology (KIT)

Wantong Huang

Karlsruhe Institute of Technology (KIT)

Johanna Matusche

Karlsruhe Institute of Technology (KIT)

Paul Greule

Karlsruhe Institute of Technology (KIT)

Jonas Arnold

Karlsruhe Institute of Technology (KIT)

Lovis Hardeweg

Karlsruhe Institute of Technology (KIT) https://orcid.org/0009-0003-1378-043X

Máté Stark

Karlsruhe Institute of Technology (KIT)

Luise Renz

Karlsruhe Institute of Technology (KIT)

Affan Safeer

Physikalisches Institut, Universität zu Köln

Daniel Jansen

Physikalisches Institut, Universität zu Köln https://orcid.org/0009-0002-0763-5853

Thomas Michely

University of Cologne https://orcid.org/0000-0003-1657-1847

Jeison Fischer

Physikalisches Institut, Universität zu Köln

Wolfgang Wernsdorfer

Karlsruhe Institute of Technology https://orcid.org/0000-0003-4602-5257

Christoph Sürgers

karlsruhe institute of technology https://orcid.org/0000-0002-2132-9775

Hannu-Pekka Komsa

University of Oulu https://orcid.org/0000-0002-0970-0957

Johannes Schwenk

Karlsruhe Institute of Technology (KIT)

Wouter Jolie

Physikalisches Institut, Universität zu Köln

Article

Keywords:

Posted Date: February 27th, 2026

DOI: https://doi.org/10.21203/rs.3.rs-8911890/v1

License: This work is licensed under a Creative Commons Attribution 4.0 International License.
Read Full License

Additional Declarations: There is **NO** Competing Interest.

Atomic-Scale Quantum Control of Single Spin Defects in a Two-Dimensional Semiconductor

Kwan Ho Au-Yeung[1,2†], Wantong Huang[1†], Johanna Matusche[1†], Paul Greule[1], Jonas Arnold[1], Lovis Hardeweg[1], Máté Stark[1], Luise Renz[1], Affan Safeer[3], Daniel Jansen[3], Thomas Michely[3], Jeison Fischer[3], Wolfgang Wernsdorfer[1,2,4], Christoph Sürgers[1], Hannu-Pekka Komsa[5], Johannes Schwenk[1*], Wouter Jolie[3*], Philip Willke[1,2]

[1] Physikalisches Institut (PHI), Karlsruhe Institute of Technology, Karlsruhe, Germany

[2] Center for Integrated Quantum Science and Technology (IQST), Karlsruhe Institute of Technology, Karlsruhe, Germany

[3] II. Physikalisches Institut, Universität zu Köln, Cologne, Germany

[4] Institute for Quantum Materials and Technologies (IQMT), Karlsruhe Institute of Technology, Karlsruhe, Germany

[5] Faculty of Information Technology and Electrical Engineering, University of Oulu, Oulu, Finland

[*] corresponding author: johannes.schwenk@kit.edu , wjolie@ph2.uni-koeln.de

[†] These authors contributed equally

Abstract

Individual spin defects in solids are promising building blocks for quantum technologies, but their deterministic creation, individual addressability, and operation near surfaces remain major challenges. Two-dimensional materials provide an attractive alternative, as their single-layer thickness enables direct atomic-scale access to defect states. Here, we demonstrate single-spin control of solid-state defects in a two-dimensional semiconductor by a combination of scanning tunneling microscopy and electron spin resonance. We create and manipulate individual sulfur vacancies and carbon substitution defects in monolayer molybdenum disulfide and characterize their spin dynamics, including coherent control, at the single-defect level. Using atomic manipulation, we further engineer and probe spin-spin interactions between defect pairs. Our results demonstrate deterministic creation, addressability, coherent manipulation, and controlled coupling of individual spin defects within a single experimental platform. This establishes atomically engineered spin defects in two-dimensional semiconductors as a versatile class of controllable solid-state quantum systems and opens a route towards tailored quantum sensing experiments.

Introduction

Solid-state spin defects provide localized and well-isolated quantum states for sensing, communication, and information processing[1,2]. Prominent examples include donor spins in silicon[3,4], nitrogen-vacancy centers in diamond[5,6], and rare-earth ions in crystalline hosts[7]. These quantum systems combine long coherence times with optical or electrical addressability, yet deterministic placement[8] as well as individual control[1] remain major challenges. Moreover, their performance often degrades near surfaces – a critical limitation for many sensing and device applications[9].

Two-dimensional (2D) materials offer an attractive alternative to conventional solid-state hosts: Their single-layer atomic thickness places defects directly at the surface and still preserve their quantum properties. In particular, 2D semiconductors such as transition metal dichalcogenides (TMDs) provide a broad range of electronic and optical behaviors, chemical tunability, and gate response[10]. Despite these advantages, coherent control of (individual) spin defects in 2D materials has remained largely unexplored. One notable exception is hexagonal boron nitride, where spin defects can be controlled via optically detected magnetic resonance[11-15]. Still, the microscopic nature of the spin defects is often difficult to determine[16]. For 2D semiconductors, the realization of spin defects as controllable quantum objects has so far been primarily limited to theoretical work[17-19].

Scanning tunneling microscopy (STM) provides atomic-scale access to defects in 2D materials and has revealed their electronic structure in great detail, particularly for defects in TMDs[20-24]. When combined with electron spin resonance (ESR), STM enables the detection[25,26] and coherent control[27-30] of individual spins on surfaces. This capability has established single spin resonance using STM as a powerful technique for atomically precise spin control with exceptional spatial, temporal, and energy resolution. Until now, however, this has been restricted to adatoms[25] and molecular spins[29,31] *on* surfaces, which greatly limits its potential for prototyping real-world solid-state device architectures.

In this work, we probe individual solid-state spin defects in a 2D semiconductor on the atomic scale: Using monolayer molybdenum disulfide (MoS_2) supported on graphene (Gr) on Ir(111), we create, characterize and coherently control individual sulfur vacancies and carbon substitution defects with atomic precision, all in one platform. We measure their spin relaxation and coherence times, demonstrate coherent Rabi and Ramsey dynamics, and engineer tunable spin-spin interactions by assembling defect dimers. Our results establish monolayer TMDs as a platform for atomically controllable solid-state spin defects and expand ESR-STM from surface-bound adatoms and molecules to genuine solid-state quantum defects.

Electronic Structure of Spin Defects in Monolayer MoS_2

Figure 1 introduces the sample system and the atomic structure of individual defect centers. Monolayer MoS_2 was grown on Gr/Ir(111) following established procedures[32,33] and transferred under ultra-high vacuum conditions from the growth chamber (Cologne) to the ESR-STM setup (Karlsruhe, $T = 50$ mK, Fig. 1a). In other works on 2D semiconductors, defect creation is realized via the growth process[21], ion sputtering[34] or adatom manipulation[24]. Here, we instead established protocols to create atomic defects locally, on-demand and *in-situ*

using high-voltage STM tip pulses[35] (see Supplementary Fig. 1 for defect creation). This results in several distinct defect types distributed across MoS_2 islands (Fig. 1b). The two most common ones are shown in Fig. 1c: a negatively charged sulfur vacancy (right, V_S^-) and a negatively charged carbon substitution (left, C_S^-).

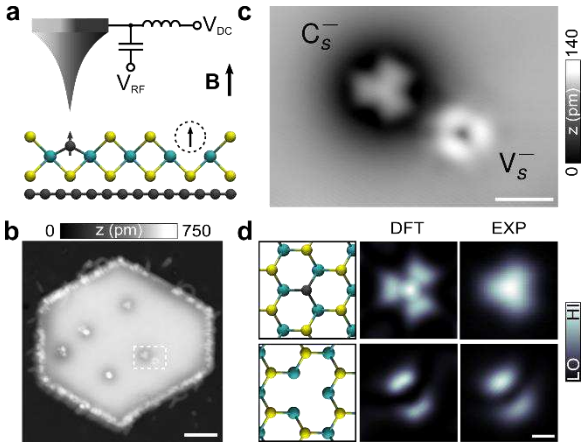


Fig. 1. Solid-state spin defects in monolayer MoS_2. a, Schematic illustration of MoS_2 on Gr/Ir(111) probed via STM (black: C; yellow: S; cyan: Mo). A carbon substitution defect (C_S^-, black) and a sulfur vacancy (V_S^-, dotted circle) are indicated with their spin. An additional RF voltage V_{RF} as well as a magnetic field is employed for ESR-STM experiments. **b**, STM image of a MoS_2 island. Multiple atomic defects are created by STM tip manipulation (scale bar: 5 nm). **c**, Close-up STM image [marked area in b] of V_S^- and C_S^- [scale bar: 1 nm; Setpoints: b-c, $V_{DC} = 1$ V, $I = 20$ pA]. **d**, Left: Top view models of the defects (Top-layer only). dI/dV orbital maps of the highest occupied defect orbital states (image size: 1.7 nm × 1.7 nm, -170 mV for V_S^- and -480 mV for C_S^-) along with corresponding DFT-calculations.

We characterize the electronic structure of the defects using scanning tunneling spectroscopy (STS) and density functional theory (DFT) calculations (Fig. 1d and Supplementary Fig. 2 and 3). In both cases, the defect orbitals result from the C_{3v} symmetry, that leads to one A_1 and two $E_{1,2}$ states with orbital degeneracy. In the case of V_S^-, spin-orbit coupling, charging, and Jahn-Teller distortion needs to be considered, which yields a highest occupied defect orbital (HODO) with a single unpaired spin in one of the $E_{1,2}$ states[20,22-24,36] while the lower lying A_1 states are fully occupied. This order is reversed in the case of C_S^- leading to a single open-shell defect configuration with one spin in the A_1 orbital. The corresponding dI/dV orbital maps of the HODOs are in excellent agreement with DFT results (Fig. 1d) and prior work[20,22-24,36,37]. Thus, while the microscopic origin of the sulfur vacancy and the carbon substitution is quite different, they both host well-defined, singly occupied defect orbitals that can serve as controllable spin $S = 1/2$ quantum states.

Magnetic Properties and Spin Dynamics of the Defect Centers

To probe the spin states of the defects, we perform magnetic-field-dependent dI/dV spectroscopy (Fig. 2a). At low voltages, these measurements show an emerging step-like feature which we attribute to inelastic electron tunneling spectroscopy (IETS) excitations from the magnetic ground state to the excited state[38]. The step position $|eV_{DC}| = g\mu_B B$ yields a g-

factor of ~2 for both spin centers (see Supplementary Fig. 4a for C_S^-). For V_S^-, the data agrees with the splitting of a Kondo resonance in magnetic fields observed in MoS_2/Au(111)[34]. Moreover, spin contrast maps (Fig. 2b; see Supplementary Fig. 4b-e for experimental details) reveal that the spatial spin density follows the shape of the HODO, leading to an extended spin signal of nearly one nanometer. According to these measurements, both defects behave as effective spin $S = 1/2$ systems with nearly-free-electron magnetic moments.

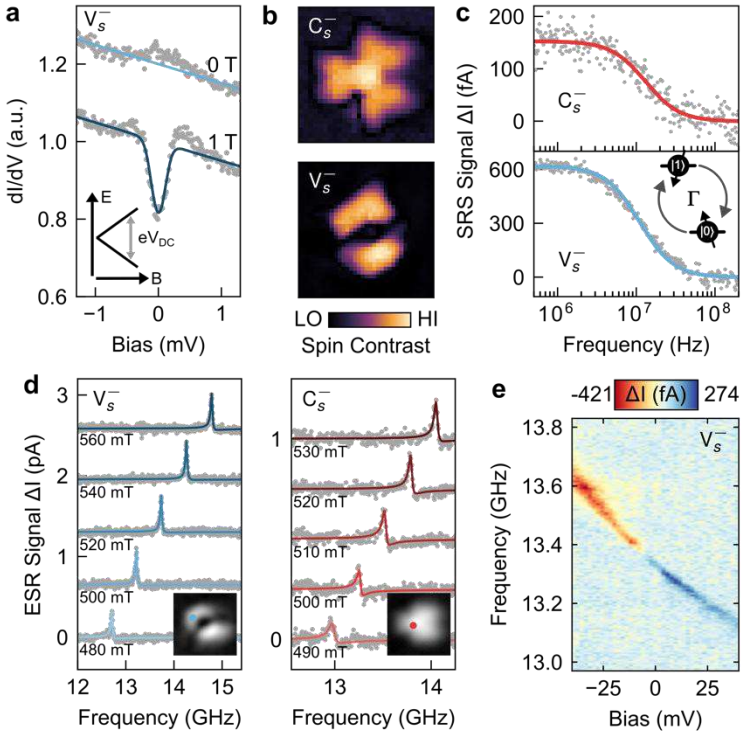


Fig. 2. Magnetic properties and spin dynamics of individual defect centers. a, dI/dV spectra of V_S^-, that show a Zeeman splitting at finite magnetic field probed via inelastic electron tunneling excitations at $|eV_{DC}| = g\mu_B B$. **b**, Spatial distribution of the spin signal of both C_S^- and V_S^- revealed by spin-contrast maps [$|d^2I/dV^2|$ acquired with a spin-polarized tip[39], 1.1 nm × 1.1 nm, see Supplementary Fig. 4b-e for details]. **c**, Stochastic resonance spectroscopy signal ΔI(f) for C_S^- (red) and V_S^- (blue). Fits to Eq. (1) yield spin relaxation rates between the ground and excited states [see inset, $\Gamma = (82 \pm 4)\ \mu s^{-1}$ for C_S^- and $(69 \pm 1)\ \mu s^{-1}$ for V_S^-]. **d**, ESR-STM spectra ΔI of single V_S^- and C_S^- at different magnetic fields (taken at positions indicated in the inset). Blue and red lines are fits to asymmetric Lorentzians. **e**, Bias-dependent ESR spectra of V_S^- acquired at constant tip height, that show electrical tuning of the resonance frequency $f_0 \propto V_{DC}$ via exchange interaction with the magnetic tip [Setpoints: a, $I = 100$ pA, $V_{DC} = 5$ mV, $V_{mod} = 50$ μV; b, $V = 10$ mV & 5 mV; $I = 200$ & 500 pA; $V_{mod} = 0.8$ & 0.5 mV; $B = 0$ T; c, $I \approx 5$ pA, $|V_{DC}| = 2$ mV, $V_{AC} = 2$ mV, $B = 0$ T; d, V_S^-: $I = 10\ pA$, $V_{DC} = 20$ mV, $V_{RF} = 5$ mV; C_S^-: $I = 5$ pA, $V_{DC} = 20$ mV, $V_{RF} = 10$ mV; e, $V_{RF} = 2$ mV, $I = 10$ pA, $V_{DC} = 20$ mV].

To quantify the spin dynamics of individual defects, we employ stochastic resonance spectroscopy (SRS)[40,41] as well as ESR-STM[25], both using magnetic STM tips (see Supplementary Note 1 for a detailed SRS analysis). In SRS, an oscillating bias voltage $V_{AC}(f)$

induces stochastic transitions between the magnetic ground and excited state, that result in a frequency-dependent change in tunneling current

$$\Delta I(f) = I_{\mathrm{SR}} \cdot \frac{\Gamma^2}{\Gamma^2+(2\pi f)^2} \quad (1)$$

where I_{SR} is the amplitude of the SRS response. This allows us to access nanosecond spin dynamics, since the spin transition rate $\Gamma \approx 1/T_1$ reflects the relaxation time T_1 (Fig. 2c)[41]. Fits to the SRS response yield relaxation times of $T_1 = (15 \pm 1)$ ns for V_S^- and $T_1 = (12 \pm 1)$ ns for C_S^-. We find that the main limitation to T_1 is the tunneling current I[42]: Γ increases with increasing I (Supplementary Fig. 5), indicating that inelastic scattering of tunneling electrons induces spin flips. In contrast, extrapolating to zero current yields current-independent relaxation rates of $\Gamma_0^{V_S^-} = (23 \pm 1)$ MHz and $\Gamma_0^{C_S^-} = (31 \pm 9)$ MHz, corresponding to relaxation times T_1 of approximately 43 ns and 32 ns, respectively. These values are likely dominated by electron scattering with the conductive Gr/Ir(111) substrate[27,42] (Supplementary Note 1).

We next perform ESR-STM measurements by detecting the change ΔI in tunneling current induced by an applied radio-frequency voltage V_{RF} as a function of radiofrequency f[25]. In Fig. 2d, a pronounced resonance peak is observed at frequency f_0, which shifts linearly with magnetic field according to

$$hf_0 = 2\mu_{\mathrm{eff}}B. \quad (2)$$

From the field dependence, we extract effective magnetic moments $\mu_{V_S^-}=(0.992 \pm 0.011)\,\mu_B$ and $\mu_{C_S^-}=(0.975 \pm 0.007)\,\mu_B$, close to the free-electron value in both cases (see Supplementary Fig. 6 for effective magnetic moments evaluation). We attribute the deviation from the latter to the residual influence of spin-orbit coupling and Kondo coupling to the substrate electron bath[43].

Finally, we demonstrate that f_0 can be locally controlled (Supplementary Note 2): In addition to tuning via the magnetic tip proximity[44,45] (Supplementary Fig. 7a), the resonance frequency can be electrically gated by the sample bias V_{DC} at constant tip height (Fig. 2e). Near the Fermi level, the shift in ESR frequency is approximately linear in V_{DC}, while pronounced nonlinearities emerge when V_{DC} approaches defect orbital resonances (Supplementary Fig. 7b-d). We attribute this behavior to transport-mediated exchange coupling between the spin defect and the tip's magnetic exchange field B_{tip}[46,47] (Supplementary Fig. 8), in which virtual hopping processes enhance the exchange interaction when the bias aligns with the spin-bearing orbitals. This mechanism, previously demonstrated for single molecules on surfaces[48], provides a viable route towards electrically gated control of solid-state spin defects.

Coherent control of a single sulfur vacancy spin

Having established the spin properties of the defect centers, we next probe the coherent dynamics of a single V_S^- spin using pulsed ESR-STM[27]: Figure 3a shows measurements of the change in tunneling current ΔI as a function of RF pulse width τ, that demonstrate coherent Rabi oscillations of the spin defect. The Rabi frequency Ω increases linearly with V_{RF} (inset;

see Methods for analysis details), consistent with single-spin control of adatoms[27] and molecules[29]. From this data, we extract a decoherence time $T_2^{\mathrm{Rabi}} = (22 \pm 1)$ ns ($V_{\mathrm{RF}} =$ 40 mV) and a minimal π-pulse duration $T_\pi^{\min} \approx 14$ ns ($V_{\mathrm{RF}} = 50$ mV). Detuning measurements further confirm coherent spin driving: mapping the Rabi sequence as a function of detuning $\delta = f\text{-}f_0$ (Fig. 3b) yields the characteristic chevron pattern and the extracted Rabi rates follow the expected relation $\Omega = \sqrt{{\Omega_0}^2 + \delta^2}$. To quantify spin relaxation and decoherence, we performed relaxometry and Ramsey experiments (Fig. 3c and d). The relaxation measurement using a two-π-pulse sequence[30] gives $T_1 = (27 \pm 3)$ ns . Ramsey fringes obtained from π/2–π/2 pulse sequences show oscillatory decay with $T_2^* = (13.5 \pm 0.6)$ ns (see Methods for analysis details). Since the lifetime remains close to those obtained by SRS (Fig. 2c), we conclude that the main limitation to T_1 is also here inelastic scattering with tunneling electrons. Concerning T_2^*, additionally dephasing is potentially introduced by the variations in the tip magnetic field[27].

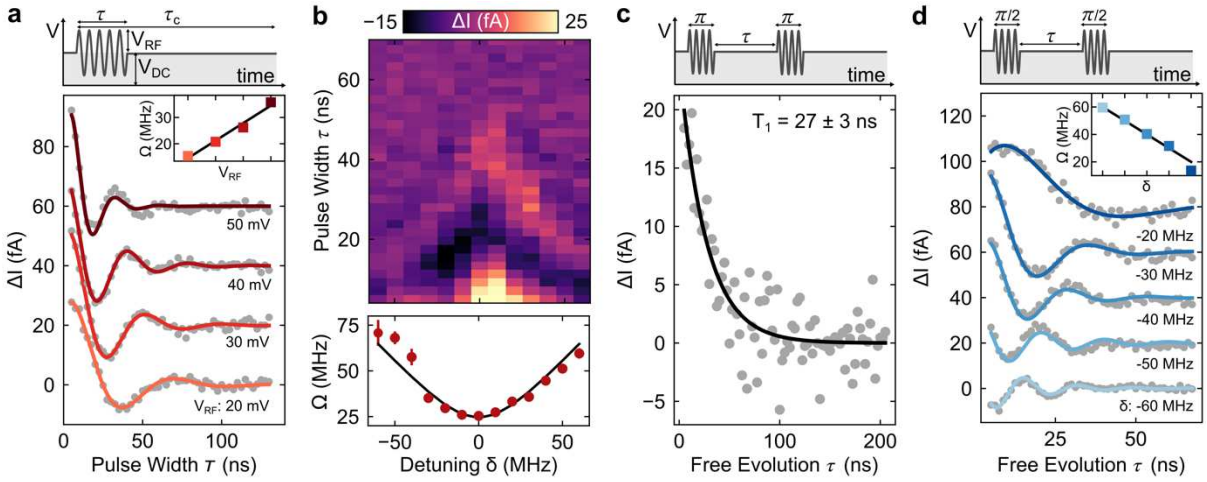


Fig. 3. Coherent control of a single sulfur vacancy spin. a, Rabi oscillation measurements on a single V_S^-. Top: Pulse scheme illustrating the DC bias V_{DC}, RF amplitude V_{RF}, RF pulse width τ and cycle time τ_c. Bottom: Change in tunneling current $\Delta I(\tau)$ for different V_{RF}. Solid lines are fits to the data (See Methods). Inset: extracted Rabi rates Ω show a linear dependence on V_{RF}. **b**, Rabi oscillations measured as a function of detuning δ=f-f_0. Top: $\Delta I(\tau, \delta)$ displaying the characteristic chevron pattern of coherent spin driving. Bottom: Extracted Rabi rates following the expected detuning dependence $\Omega(\delta)$=$\sqrt{\Omega_0^2+\delta^2}$ (solid line). **c**, Spin relaxometry measurement. Top: Pulse scheme using two π-pulses separated by a free evolution time τ. Bottom: ΔI(τ) with an exponential fit yielding a spin relaxation time T_1=(27 ± 3) ns. **d**, Ramsey interference measurement. Top: Pulse scheme. Bottom: $\Delta I(\tau)$ for different detuning δ, showing oscillatory decay of the Ramsey fringes. Fits yield an average dephasing time $T_2^* = (13.5 \pm 0.6)$ ns, (See Methods). Inset: Extracted oscillation frequencies Ω as a function of δ (colors indicating the detuning) matching the expected linear dependence (black line) [Setpoints: All measurements were performed in open loop with B=527 mT, I = 4.5 pA, V_{DC} = 20 mV and f_0 = 14.1 GHz ; $V_{RF} = 40$ mV for b-d; a-b, τ_c=250 ns ; c, τ_c=600 ns, τ_π=22 ns; d, $\tau_c = 150$ ns, $\tau_{\pi/2} = 11$ ns].

Engineering spin-spin interactions in defect dimers

Lastly, we utilize the atomic precision of STM to engineer defect dimers via tip-assisted manipulation (Supplementary Fig. 1) and to investigate their magnetic coupling: We assemble pairs of C_S^- on well-defined lattice sites and probe their mutual spin-spin interaction using ESR-STM and IETS (Fig. 4). For sufficiently separated defects in a (2,2) configuration (given in multiples of the MoS_2 lattice vectors), the system behaves as two weakly interacting $S = 1/2$ spins (Fig. 4a). ESR-STM reveals two distinct resonance peaks, consistent with additional Heisenberg exchange interaction described by $H_{ex} = J\,S_1 \cdot S_2$. In the present case, the (ferromagnetic) exchange $J \approx -400$ MHz (~ -2 μeV) is small compared to the Zeeman energy, a typical regime for coupled two-qubit systems. This leads to a frequency splitting of $\Delta f = |J|/h$, which can be interpreted as an effective field generated by the remote defect switching between its two possible spin orientations (Fig. 4a inset, Supplementary Fig. 9 and Supplementary Note 4). When the defects are positioned in a (1,3) configuration (Fig. 4b), the exchange interaction increases significantly and reaches $J \approx +354$ μeV. At this magnitude, the exchange becomes directly visible in dI/dV spectra as IETS excitations (Fig. 4b inset), which unlike in Fig. 2a persist even in the absence of magnetic field B. Notably, the increase in J occurs despite a larger absolute geometric separation between the C_S^- defects: Since the orbital overlap is increased in this angle, the magnetic exchange is increased as well.

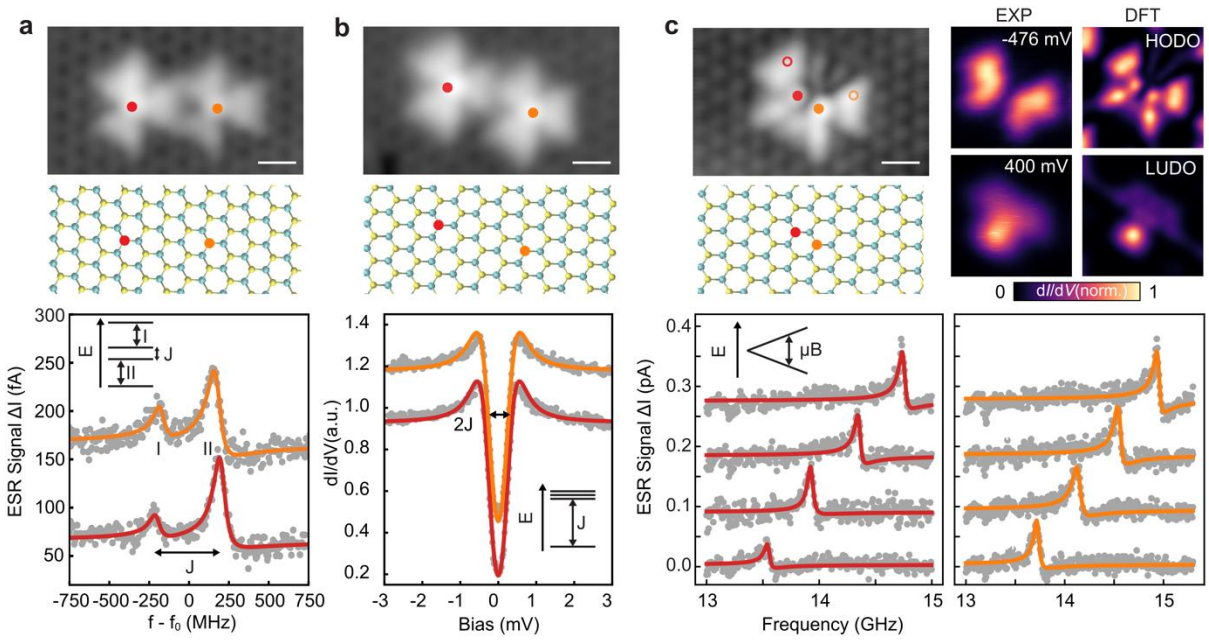


Fig. 4. Engineering spin-spin interaction in carbon substitution dimers. a – c, Atomic-scale assembly and magnetic characterization of C_S^- with different separations. Top: STM topographies (scale bars: 0.5 nm); middle: atomic models; bottom: spectroscopic signatures. **a**, For a weakly coupled dimer in a (2,2) configuration, ESR-STM reveals two distinct resonances corresponding to individual spins, split by a small (ferromagnetic) exchange interaction J of ~ -400 MHz (inset, see also Supplementary Fig. 9). **b**, For a (1,3) configuration, the interaction increases drastically to $J = 354$ μeV, which becomes directly visible as IETS in low-bias dI/dV. **c,** At the closest possible (0,1) configuration, strong orbital overlap and on-site Coulomb repulsion led to the formation of a new electronic state, $(2C_S)^-$, hosting a single

unpaired electron. Constant-height dI/dV maps and DFT calculations reveal modified orbitals (upper right), while ESR-STM (bottom left and right) detects the response of a single isolated spin $S = 1/2$ without exchange splitting (Spectra are taken at the open circle positions to emphasize the delocalized nature of the defect spin). Thus, $(2C_S)^-$ mimics the formation of a hydrogen molecule ion and gives rise to emergent states beyond a coupled-spin model. [Setpoints: a, $I = 30$ pA, $V_{DC} = 30$ mV, $V_{RF} = 10$ mV, $B = 520$ mT, $f_0 = 14.264$ / 14.222 GHz; b, $I = 200$ pA, $V_{DC} = 10$ mV, $V_{mod} = 40$ µV, $B = 0$ T; c, Bottom left: $I =$ 10 pA, $V_{DC} = 30$ mV, $V_{RF} = 12$ mV, Bottom right: $I = 15$ pA, $V_{DC} = 30$ mV, $V_{RF} = 10$ mV. Difference of $\Delta f \sim 200$ MHz between the two measurements is attributed to the residual tip magnetic field[45]].

A qualitatively different regime is reached for the closest possible configuration, (0,1), shown in Fig. 4c. Here, magnetic-field-dependent ESR-STM spectra acquired at different positions (Fig. 4c, bottom) exhibit the response of a single isolated $S = 1/2$ spin [$\mu_{(2C_S)^-} = (0.975 \pm 0.004)\ \mu_B$], with no observable exchange splitting. Consistently, no IETS signal is detected in dI/dV in zero magnetic field. To shed light on the origin of these results, we performed dI/dV maps of the HODO and LUDO (Fig. 4c, upper right; see Supplementary Fig. 10a,b for dI/dV spectrum and additional maps). These maps reveal orbital shapes that differ markedly from those of isolated C_S^- defects (Fig. 1d). DFT calculations (Supplementary Fig. 10c-e and Supplementary Note 3) show that this is a combined effect of strong orbital overlap and large on-site Coulomb repulsion, which lead to a change in the orbital structure. This also suppresses double occupancy, which leaves only a single electron localized on the dimer, rationalizing the ESR measurements. As a result, the new defect $(2C_S)^-$ undergoes a qualitative transition characterized by orbital states that are distinct from those of its two C_S^- constituents. In close analogy to the formation of the hydrogen molecule ion H_2^+ from two hydrogen atoms, $(2C_S)^-$ constitutes an electronically and magnetically distinct entity rather than a strongly coupled spin pair.

Discussion

A central challenge for future progress is to further enhance spin coherence. While coherent manipulation is already achieved, prolonging spin lifetimes will require to reduce inelastic electron scattering, that stems from the presence of the tunneling current and proximity to the conducting electrodes. On the detection side, this can be addressed by remote spin readout schemes[28] or by force-based detection[49] that decouple spin readout from electronic transport. On the materials side, substrate-induced relaxation can be mitigated by introducing additional non-conductive decoupling layers (e.g. bilayer MoS_2 or hexagonal boron nitride), by employing insulating substrates such as silicon carbide[22,23] or by using freestanding MoS_2[50].

Equally important is the deterministic creation and placement of defects using STM-based atom manipulation. This capability opens a route toward atomically engineered spin structures in two dimensions, analogous to phosphorus donor-based architectures in silicon[8], but with the additional advantage of *in-situ* tuning, characterization, and control at the single-spin level. In this context, extending ESR-STM from adatoms and molecular spins to solid-state spin defects

significantly broadens its scope and establishes it as a general tool for coherent control in complex solid-state systems.

More generally, the combination of atomic-scale addressability, engineered spin-spin interactions, and surface accessibility makes spin defects in 2D materials particularly well-suited for integration into functional nanoscale devices. These attributes provide a foundation for exploring nanoscale quantum sensing, engineered spin networks, and model quantum systems. Together, our results position spin defects in 2D materials as a viable platform for solid-state quantum nanotechnologies.

Methods

Sample preparation

Monolayer MoS_2 on graphene/Ir(111) is prepared by molecular beam epitaxy in an ultrahigh-vacuum (UHV) chamber (base pressure = 1×10^{-10} mbar). First, Ir(111) is cleaned by cycles of 1 keV Ar^+ ion sputtering and flash annealing to 1510 K. To obtain single layer graphene on Ir(111), clean Ir(111) is exposed to 1×10^{-7} mbar ethylene at room temperature for 120 s. Afterwards, the sample is shortly annealed to 1470 K without ethylene. Subsequently, the sample is exposed to 3×10^{-7} mbar ethylene at 1370 K for 600 s to obtain a full graphene monolayer on Ir(111)[51]. The sample is then exposed to a Mo flux from an e-beam evaporator simultaneously with a S flux obtained by decomposing pyrite (FeS_2) in a Knudsen cell (distance ~8 cm). The S flux is characterized by a distant ion gauge measuring a S pressure of 1×10^{-8} mbar. The sample is subsequently annealed at 1000 K for 300 s in the same sulfur flux, following Ref. [52].

For ESR-STM measurements, the sample is transferred from the preparation chamber to the ESR-STM chamber using an ultrahigh vacuum suitcase (base pressure = 5×10^{-10} mbar). All measurements were done in a Unisoku USM1600 STM inside a homebuilt dilution refrigerator with a base temperature of 50 mK.

Spin polarized tips

Fe atom deposition is carried out by electron-beam evaporation (3 s, ion current ~5 nA at ~30 cm distance) onto the cooled (<100 K) MoS_2/(Gr)/Ir(111) sample. All ESR and SRS experiments were carried out using spin-polarized tips. These were prepared by transferring individual Fe adatoms adsorbed on either graphene or MoS_2 onto the PtIr tip by STM vertical atom manipulation. Spin polarization was then verified through the asymmetry in dI/dV measurements around zero bias on V_S^- or C_S^- defects (Supplementary Fig. 4b-e). Note that while the bias voltage was applied to the STM tip, all bias signs were inverted in the manuscript to follow the conventional definition of bias voltage with respect to the sample bias.

ESR and pulsed ESR

The RF voltage was added to the tip side of the junction via a cryogenic diplexer (Marki Microwave MDPX-0305) located at the 1 K stage of the cryostat using an RF generator (Anritsu MG3694C). For pulsed ESR measurements, we followed the pulse schemes introduced in Ref. [27]. The continuous wave RF signal from the RF generator was used as the

local oscillator of an IQ mixer (Marki MMIQ0626H). Time-dependent $I(t)$ and $Q(t)$ from an arbitrary waveform generator (Zurich Instruments HDAWG) drove the I and Q ports to gate the RF signal and apply phase-coherent pulse sequences (π or π/2 pulses). A 3-dB attenuator was added (at room temperature) before the cryogenic diplexer. The ESR signal in the tunnelling current was read out with a digital lock-in (Stanford Research Systems SR860) using on/off modulation at 323 Hz. The RF pulses were only present in the Lockin A-cycle. Therefore, the measured signal presents an average of the spin state-related tunnel current. The DC background is applied over the whole cycle time τ_c. we applied pulse sequences with on-time τ and off-time τ_{off} keeping the sum ($\tau_{\mathrm{c}} = \tau + \tau_{\mathrm{off}}$) fixed.

Rabi oscillations were analyzed by using a damped cosine model (solid line in Fig. 3a) with an exponential envelope, $\Delta I(\tau) = A \cdot \cos(2\pi\Omega\tau+\phi)\ \exp\left[-\tau/T_2^{\mathrm{Rabi}}\right]$. Here, τ is the pulse width, A is the maximum change in current and T_2^{Rabi} is the Rabi decoherence time. A linear background caused by current rectification with increasing τ was subtracted from the data [27]. Rabi frequency Ω extracted from the fits as a function of V_{RF}. T_2^{Rabi} was then extracted from the fits in Fig. 3a.

Ramsey interference measurements were analyzed by using the standard Ramsey model (solid line in Fig. 3d) $\Delta I(\tau) = A \cdot \cos\left(2\pi\Omega\tau + \phi\right) \exp\left(-\tau/T_2^*\right) + I_0$, where A is the amplitude, ϕ a phase offset, and T_2^* the inhomogeneous dephasing time. Oscillation frequencies Ω extracted from the fits as a function of detuning δ. T_2^* was then extracted as a function of detuning.

SRS measurements

For SRS measurements, the low-frequency offset voltage was combined with the high-frequency modulation using an external bias-tee (Mini-circuits ZFBT-6GW+) and it was applied to the tip-side of the tunnel junction via the low frequency input of the cryogenic diplexer. The AC modulation signal was produced by an arbitrary waveform generator (Zurich Instruments HDAWG). The SRS signal was read out with a digital lock-in (Stanford Research Systems SR860) using on/off modulation at 323 Hz.

Computational methods

Density functional theory (DFT) calculations are all performed within the projector-augmented wave formalism implemented in the VASP software package [53-55]. For the presented results in the figures, Heyd-Scuseria-Ernzerhof (HSE06) hybrid functionals and a mixing parameter of 10% were used [56,57]. This was found to yield energy differences between occupied and unoccupied defect states, in closer agreement with experiments, as compared to e.g. those from the Perdew-Burke-Ernzerhof (PBE) functional [58] or HSE06 with standard mixing parameter of 25%. Hybrid functionals also improve on the predicted band gap value, which is found to be 1.91 eV for HSE-10%. A plane-wave basis with a 500 eV cutoff was employed. Both defects were modeled within a 6×6 supercell and the Brillouin zone was sampled using a 2×2 k-point-mesh. The structural relaxations were carried out in spin-polarized form, followed by single-shot non-collinear calculations with spin-orbit coupling. STM images were simulated using Tersoff-Hamann approach [59], essentially corresponding to evaluation of a local DOS. In

practice, the squared wave functions of defect states were extracted using the VASPKIT package [60], and from that we took a plane at a constant height from the surface.

References

1 Wolfowicz, G. *et al.* Quantum guidelines for solid-state spin defects. *Nature Reviews Materials* **6**, 906-925 (2021). https://doi.org/10.1038/s41578-021-00306-y

2 Awschalom, D. D., Bassett, L. C., Dzurak, A. S., Hu, E. L. & Petta, J. R. Quantum Spintronics: Engineering and Manipulating Atom-Like Spins in Semiconductors. *Science* **339**, 1174-1179 (2013). https://doi.org/doi:10.1126/science.1231364

3 Morello, A. *et al.* Single-shot readout of an electron spin in silicon. *Nature* **467**, 687-691 (2010). https://doi.org/10.1038/nature09392

4 Watson, T. F. *et al.* Atomically engineered electron spin lifetimes of 30 s in silicon. *Science Advances* **3**, e1602811 (2017). https://doi.org/doi:10.1126/sciadv.1602811

5 Balasubramanian, G. *et al.* Nanoscale imaging magnetometry with diamond spins under ambient conditions. *Nature* **455**, 648-651 (2008). https://doi.org/10.1038/nature07278

6 Thiel, L. *et al.* Probing magnetism in 2D materials at the nanoscale with single-spin microscopy. *Science* **364**, 973-976 (2019). https://doi.org/doi:10.1126/science.aav6926

7 Yin, C. *et al.* Optical addressing of an individual erbium ion in silicon. *Nature* **497**, 91-94 (2013). https://doi.org/10.1038/nature12081

8 Kiczynski, M. *et al.* Engineering topological states in atom-based semiconductor quantum dots. *Nature* **606**, 694-699 (2022). https://doi.org/10.1038/s41586-022-04706-0

9 Marchiori, E. *et al.* Nanoscale magnetic field imaging for 2D materials. *Nature Reviews Physics* **4**, 49-60 (2022). https://doi.org/10.1038/s42254-021-00380-9

10 Liu, X. & Hersam, M. C. 2D materials for quantum information science. *Nature Reviews Materials* **4**, 669-684 (2019). https://doi.org/10.1038/s41578-019-0136-x

11 Gottscholl, A. *et al.* Initialization and read-out of intrinsic spin defects in a van der Waals crystal at room temperature. *Nature Materials* **19**, 540-545 (2020). https://doi.org/10.1038/s41563-020-0619-6

12 Chejanovsky, N. *et al.* Single-spin resonance in a van der Waals embedded paramagnetic defect. *Nature Materials* **20**, 1079-1084 (2021). https://doi.org/10.1038/s41563-021-00979-4

13 Stern, H. L. *et al.* A quantum coherent spin in hexagonal boron nitride at ambient conditions. *Nature Materials* **23**, 1379-1385 (2024). https://doi.org/10.1038/s41563-024-01887-z

14 Gao, X. *et al.* Single nuclear spin detection and control in a van der Waals material. *Nature* **643**, 943-949 (2025). https://doi.org/10.1038/s41586-025-09258-7

15 Whitefield, B. *et al.* Narrowband quantum emitters in hexagonal boron nitride with optically addressable spins. *Nature Materials* (2026). https://doi.org/10.1038/s41563-025-02458-6

16 Mendelson, N. *et al.* Identifying carbon as the source of visible single-photon emission from hexagonal boron nitride. *Nature Materials* **20**, 321-328 (2021). https://doi.org/10.1038/s41563-020-00850-y

17 Li, S., Thiering, G., Udvarhelyi, P., Ivády, V. & Gali, A. Carbon defect qubit in two-dimensional WS_2. *Nature Communications* **13**, 1210 (2022). https://doi.org/10.1038/s41467-022-28876-7

18 Tsai, J.-Y., Pan, J., Lin, H., Bansil, A. & Yan, Q. Antisite defect qubits in monolayer transition metal dichalcogenides. *Nature Communications* **13**, 492 (2022). https://doi.org/10.1038/s41467-022-28133-x

19 Lee, Y. *et al.* Spin-defect qubits in two-dimensional transition metal dichalcogenides operating at telecom wavelengths. *Nature Communications* **13**, 7501 (2022). https://doi.org/10.1038/s41467-022-35048-0

20 Aliyar, T. *et al.* Symmetry Breaking and Spin–Orbit Coupling for Individual Vacancy-Induced In-Gap States in MoS_2 Monolayers. *Nano Letters* **24**, 2142-2148 (2024). https://doi.org/10.1021/acs.nanolett.3c03681

21 Schuler, B. *et al.* How substitutional point defects in two-dimensional WS_2 induce charge localization, spin–orbit splitting, and strain. *ACS Nano* **13**, 10520-10534 (2019). https://doi.org/10.1021/acsnano.9b04611

22 Schuler, B. *et al.* Large Spin-Orbit Splitting of Deep In-Gap Defect States of Engineered Sulfur Vacancies in Monolayer WS_2 *Physical Review Letters* **123**, 076801 (2019). https://doi.org/10.1103/PhysRevLett.123.076801

23 Schuler, B. *et al.* Electrically driven photon emission from individual atomic defects in monolayer WS_2. *Science Advances* **6**, eabb5988 (2020). https://doi.org/doi:10.1126/sciadv.abb5988

24 Jansen, D. *et al.* Tip-induced creation and Jahn-Teller distortions of sulfur vacancies in single-layer MoS_2. *Physical Review B* **109**, 195430 (2024). https://doi.org/10.1103/PhysRevB.109.195430

25 Baumann, S. *et al.* Electron paramagnetic resonance of individual atoms on a surface. *Science* **350**, 417-420 (2015). https://doi.org/doi:10.1126/science.aac8703

26 Willke, P. *et al.* Probing quantum coherence in single-atom electron spin resonance. *Science Advances* **4**, eaaq1543 (2018). https://doi.org/doi:10.1126/sciadv.aaq1543

27 Yang, K. *et al.* Coherent spin manipulation of individual atoms on a surface. *Science* **366**, 509-512 (2019). https://doi.org/doi:10.1126/science.aay6779

28 Wang, Y. *et al.* An atomic-scale multi-qubit platform. *Science* **382**, 87-92 (2023). https://doi.org/doi:10.1126/science.ade5050

29 Willke, P. *et al.* Coherent Spin Control of Single Molecules on a Surface. *ACS Nano* **15**, 17959-17965 (2021). https://doi.org/10.1021/acsnano.1c06394

30 Kovarik, S. *et al.* Spin torque–driven electron paramagnetic resonance of a single spin in a pentacene molecule. *Science* **384**, 1368-1373 (2024). https://doi.org/doi:10.1126/science.adh4753

31 Zhang, X. *et al.* Electron spin resonance of single iron phthalocyanine molecules and role of their non-localized spins in magnetic interactions. *Nature Chemistry* **14**, 59-65 (2022). https://doi.org/10.1038/s41557-021-00827-7

32 N'Diaye, A. T., Coraux, J., Plasa, T. N., Busse, C. & Michely, T. Structure of epitaxial graphene on Ir(111). *New Journal of Physics* **10**, 043033 (2008). https://doi.org/10.1088/1367-2630/10/4/043033

33 Hall, J. *et al.* Molecular beam epitaxy of quasi-freestanding transition metal disulphide monolayers on van der Waals substrates: a growth study. *2D Materials* **5**, 025005 (2018). https://doi.org/10.1088/2053-1583/aaa1c5

34 Trishin, S., Lotze, C., Krane, N. & Franke, K. J. Electronic and magnetic properties of single chalcogen vacancies in MoS_2/Au(111). *Physical Review B* **108**, 165414 (2023). https://doi.org/10.1103/PhysRevB.108.165414

35 Hosoki, S., Hosaka, S. & Hasegawa, T. Surface modification of MoS_2 using an STM. *Applied Surface Science*, 643-647 (1992). https://doi.org/https://doi.org/10.1016/0169-4332(92)90489-K

36 Xiang, F. *et al.* Charge state-dependent symmetry breaking of atomic defects in transition metal dichalcogenides. *Nature Communications* **15**, 2738 (2024). https://doi.org/10.1038/s41467-024-47039-4
37 Cochrane, K. A. *et al.* Spin-dependent vibronic response of a carbon radical ion in two-dimensional WS_2. *Nature Communications* **12**, 7287 (2021). https://doi.org/10.1038/s41467-021-27585-x
38 Ternes, M. Spin excitations and correlations in scanning tunneling spectroscopy. *New Journal of Physics* **17**, 063016 (2015). https://doi.org/10.1088/1367-2630/17/6/063016
39 Huang, W. *et al.* Quantum spin-engineering in on-surface molecular ferrimagnets. *Nature Communications* **16**, 5208 (2025). https://doi.org/10.1038/s41467-025-60409-w
40 Hänze, M. *et al.* Quantum stochastic resonance of individual Fe atoms. *Science Advances* **7**, eabg2616 (2021). https://doi.org/doi:10.1126/sciadv.abg2616
41 Betz, N. *et al.* Stochastic Resonance Spectroscopy: Characterizing Fast Dynamics with Slow Measurements. *arXiv preprint arXiv:2412.12647* (2024).
42 Paul, W. *et al.* Control of the millisecond spin lifetime of an electrically probed atom. *Nature Physics* **13**, 403-407 (2017). https://doi.org/10.1038/nphys3965
43 Bagchi, M. *et al.* Spin-Polarized Scanning Tunneling Microscopy Measurements of an Anderson Impurity. *Physical Review Letters* **133**, 246701 (2024). https://doi.org/10.1103/PhysRevLett.133.246701
44 Yang, K. *et al.* Tuning the Exchange Bias on a Single Atom from 1 mT to 10 T. *Physical Review Letters* **122**, 227203 (2019). https://doi.org/10.1103/PhysRevLett.122.227203
45 Willke, P., Yang, K., Bae, Y., Heinrich, A. J. & Lutz, C. P. Magnetic resonance imaging of single atoms on a surface. *Nature Physics* **15**, 1005-1010 (2019). https://doi.org/10.1038/s41567-019-0573-x
46 Braun, M., König, J. & Martinek, J. Theory of transport through quantum-dot spin valves in the weak-coupling regime. *Physical Review B* **70**, 195345 (2004). https://doi.org/10.1103/PhysRevB.70.195345
47 Reina-Gálvez, J. *et al.* Efficient driving of a spin qubit using single-atom magnets. *Physical Review Research* **7**, L042055 (2025). https://doi.org/10.1103/qpz5-s6fw
48 Greule, P. *et al.* Spin-electric control of individual molecules on surfaces. *arXiv preprint arXiv:2507.13699* (2025). https://doi.org/https://doi.org/10.48550/arXiv.2507.13699
49 Sellies, L. *et al.* Single-molecule electron spin resonance by means of atomic force microscopy. *Nature* **624**, 64-68 (2023). https://doi.org/10.1038/s41586-023-06754-6
50 Krane, N., Lotze, C., Läger, J. M., Reecht, G. & Franke, K. J. Electronic Structure and Luminescence of Quasi-Freestanding MoS_2 Nanopatches on Au(111). *Nano Letters* **16**, 5163-5168 (2016). https://doi.org/10.1021/acs.nanolett.6b02101
51 Coraux, J. *et al.* Growth of graphene on Ir(111). *New Journal of Physics* **11**, 023006 (2009). https://doi.org/10.1088/1367-2630/11/2/023006
52 Ehlen, N. *et al.* Narrow photoluminescence and Raman peaks of epitaxial MoS_2 on graphene/Ir(1 1 1). *2D Materials* **6**, 011006 (2019). https://doi.org/10.1088/2053-1583/aaebd3
53 Kresse, G. & Hafner, J. Ab initio molecular dynamics for liquid metals. *Physical Review B* **47**, 558-561 (1993). https://doi.org/10.1103/PhysRevB.47.558
54 Kresse, G. & Furthmüller, J. Efficiency of ab-initio total energy calculations for metals and semiconductors using a plane-wave basis set. *Computational Materials*

Science **6**, 15-50 (1996). https://doi.org/https://doi.org/10.1016/0927-0256(96)00008-0

55 Kresse, G. & Furthmüller, J. Efficient iterative schemes for ab initio total-energy calculations using a plane-wave basis set. *Physical Review B* **54**, 11169-11186 (1996). https://doi.org/10.1103/PhysRevB.54.11169

56 Heyd, J., Scuseria, G. E. & Ernzerhof, M. Hybrid functionals based on a screened Coulomb potential. *The Journal of Chemical Physics* **118**, 8207-8215 (2003). https://doi.org/10.1063/1.1564060

57 Krukau, A. V., Vydrov, O. A., Izmaylov, A. F. & Scuseria, G. E. Influence of the exchange screening parameter on the performance of screened hybrid functionals. *The Journal of Chemical Physics* **125** (2006). https://doi.org/10.1063/1.2404663

58 Perdew, J. P., Burke, K. & Ernzerhof, M. Generalized Gradient Approximation Made Simple. *Physical Review Letters* **77**, 3865-3868 (1996). https://doi.org/10.1103/PhysRevLett.77.3865

59 Tersoff, J. & Hamann, D. R. Theory of the scanning tunneling microscope. *Physical Review B* **31**, 805-813 (1985). https://doi.org/10.1103/PhysRevB.31.805

60 Wang, V., Xu, N., Liu, J.-C., Tang, G. & Geng, W.-T. VASPKIT: A user-friendly interface facilitating high-throughput computing and analysis using VASP code. *Computer Physics Communications* **267**, 108033 (2021). https://doi.org/https://doi.org/10.1016/j.cpc.2021.108033

Acknowledgments

P.W. acknowledges funding from the Emmy Noether Programme of the Deutsche Forschungsgemeinschaft (DFG, WI5486/1-2). P.G. and P.W. acknowledge financial support from the Hector Fellow Academy (Grant No. 700001123). P.W. and K.H.A.Y. acknowledge support from the Center for Integrated Quantum Science and Technology (IQST). P.W., J.S., J.A., L.H. and L.R. acknowledge funding from the ERC Starting Grant ATOMQUANT. W.J. acknowledges funding from the DFG through priority program SPP2244 (Project No. 535290457). W.J. and T.M. acknowledge funding from DFG through CRC1238 (project number 277146847, subprojects A01 and B06).

Contributions

P.W., W.J and J.S. conceived the experiment. K.H.A.Y, W.H., J.M., P.G., J.A., L.H., M.S., L.R., J.S., C.S., W.W. and P.W. set up the experiment and conducted the ESR-STM measurements. W.J., A.S., D.J., J.F., T.M. prepared the sample, K.H.A.Y, W.H., J.M., P.G., J.A., L.H., M.S., L.R., J.S., W.J., A.S., D.J., J.F analyzed the experimental data. H.P.K. performed the DFT calculations. P.W., K.H.A.Y, W.H., J.M., P.G., J.A., J.S., D.J., H.P.K. and W.J. wrote the manuscript with input from all authors. P.W., W.J. and J.S. supervised the project.

Competing interests

The authors declare no competing interests.

Supplementary Files

This is a list of supplementary files associated with this preprint. Click to download.

- SupplementAtomicScaleQuantumControlofIndividualSpinDefectsinaTwoDimensionalSemiconductor20260218.docx